Response of vacuum vessel inner shell under low-speed impact

ZHAI Hua[1,a] *, WANG Xuncheng[1,b], LI Cheng[1,c], MA Jianguo[2,d],
LIU Zhihong[2,e] * and WU Yucheng[1,f]

[1]Anhui Province Key Lab of Aerospace Structural Parts Forming Technology and Equipment, Hefei University of Technology, Hefei, China

[2]Institute of Plasma Physics, Chinese Academy of Sciences, Hefei, China

[a]jxzhaihuajx@hfut.edu.cn, [b]1542365788@qq.com, [c]963734268@qq.com, [d]mjg@ipp.ac.cn, [e]zhliu@ipp.ac.cn, [f]ycwu@hfut.edu.cn

Abstract. Nuclear fusion energy is a promising new energy, This vacuum environment in nuclear fusion reactor is provided by the precision vacuum vessel, which also provides a support structure for the installation of internal components of the fusion device. In this paper, the impact response of double layer vacuum chamber inner wall under transverse impact load is experimentally studied to manufacture the high quality vacuum chamber. From the drop weight experiments, the vacuum chamber wall under five groups of different impact energy is analyzed, and the impact response displacement, and energy absorption rate of the sample are compared and discussed. The experimental results show that the impact force and impact response displacement increase with the impact energy, and the error also increases. The influence of rib plate in the vacuum chamber inner wall on impact response displacement is analyzed. With the increase of the damage deformation of the vacuum chamber wall, the rebound amount of the impact block cannot increase linearly with the impact energy. The actual situation is simulated with software, and the results of experimental and simulated energy absorption are compared and explained.

Introduction

Nuclear fusion energy is a promising new energy [1]. In order to realize controllable nuclear fusion reaction, it is necessary to provide a very high vacuum environment to ensure the operation of plasma [2,3]. This vacuum environment is provided by the vacuum vessel with D-shaped ring structure through full penetration welding, which also provides a support structure for the installation of internal components of the fusion device. The design of the double shell structure can be filled with boron containing screen cooling water with shielding function. The whole annular vacuum vessel structure is divided into 8 sectors, and 1/8 sector is divided into 1/16 sector. 1/16 sector consist of multiple PS1-PS4 sections [4]. In the welding process, the internal stress caused by thermal expansion and cold contraction will lead to plastic shrinkage deformation. Reasonable welding sequence can reduce large shrinkage residual stress, and achieve the effect of reducing welding deformation. Keimasaki et al. [5] proposed the assembly sequence for the JT-60sa vacuum vessel. Xu et al. [6] further predicted the deformation of vacuum vessels based on inherent strain theory, and proposed six different welding sequences of PS3 section, and obtained the optimal results. They also obtained the conclusion that applying external constraints will significantly reduce welding deformation, but the welding residual stress will increase, and the annular stiffener has the function of restraining welding deformation. Chen et al. [7] proposed a thermo-elasto-plastic finite element method using shell element with section integration to study the influence of welding sequence on the structural deformation and residual stress of large stiffened plates. Ordieres J. [8] investigated the influence of welding fixture on welding

deformation of ITER vacuum vessel PS1 by finite element method, the control effect of welding fixture on welding deformation is better than that of welding sequence.

The heat input of various welding methods is quite different, and under the condition of using the same welding method, different joint forms have different effects on the longitudinal, transverse and angular deformation. Ji et al. [9] studied the influence of narrow gap tungsten inert gas welding (ng-tig) and electronic restraint welding (EBW) on the welding results in the manufacturing process of CFETR by using nondestructive testing technology and mechanical tests. The impact absorption energy of the two welded joints is lower than that of the base metal, but the strength of ng-tig weld is higher than that of the base metal. P. Y.lee et al. [10] proposed all parts into a whole through bolts and shear keys. The finite element analysis shows that the maximum static stress intensity of the structure without welding is within the stress limit, and there will be no large deformation and stress concentration. At the same time, the fatigue life of the new structure is much higher than the design standard of ITER. Zhai et al. [11] used electron beam welding technology to prepare welded joints with different weld spacing, and studied the microstructure and mechanical properties under different weld spacing. The results showed that the grain size in the heat affected zone increased with the increase of weld spacing, and the joint with small weld spacing after welding had better performance.

The welding tooling of large structural parts mainly ensures the accuracy through fixtures and adjusting devices. Li et al. [12] calculated the mathematical optimization model of the position deviation of the clamping part according to the geometric relationship between the resultant force of all external forces on the clamping part in the spatial coordinate system and the total contact stiffness. Based on inherent strain theory, Ji et al. [13] analyzed the welding deformation of 1/32 vacuum vessel, the welding fixture and the reserved allowance for welding shrinkage were used to reduce the welding deformation. It is often necessary to detect the welding quality of the vacuum vessel sector according to the problems of weld surface cracks, incomplete penetration, weld leakage and workpiece surface cracks. Wang et al. [14] designed a dual matrix array probe to solve the limitations of the traditional ultrasonic testing, and used ultrasonic testing technology to carry out non-destructive testing of CFETR welding [15]. Yutonoguchi et al. [16] Evaluated the applicability of eddy current testing method to detect the welding defects of hydraulic pipes of ITER cladding module. G D'Amico et al. [17] predicted the mechanical behavior to control the fixture forces generated in the welding process. Caixas et al. [18] established a welding vacuum vessel thermal load model, compared the actual and accurate deformation with the simulation results. Zhang et al. [19] concluded that the largest deformation in the welding process occurred on the shell around the transition structure, and the main difference between welding stress and deformation occurred at the shell around the window.

Some relevant work have been performed to reduce the welding deformation of the vacuum vessel , but there is relatively little research on how to straighten the deformation after welding. In this paper, a low speed impact experiment device for the vacuum inner shell is designed. Through the impact response analysis of the vacuum inner shell after impact, the deformation caused by the inner wall after welding can be reduced to improve inconvenient manual operation and low efficiency, and provides a design basis for the further research and development of the vacuum vessel welding deformation straightening correction device.

Experimental research

Experimental specimen and low speed impact device. Due to the huge volume of the vacuum vessel, it needs a lot of materials to manufacture the equal scale model, and the process degree becomes correspondingly complex with the increase of the size in the processing and manufacturing process. Therefore, the samples in this experiment are scaled to produce the vacuum inner shell model. The samples size were reduced by 5 times. The vacuum inner shell becomes 10mm, and the total length and width will be reduced accordingly. The material is 316L stainless

steel, whose performance parameters are shown in Table 1, which is convenient for processing and manufacturing and correction experiments.

Table 1. 316L stainless steel performance parameters.

Material	E(GPa)	μ	σ_s (MPa)	G (MPa)
316L	210	0.288	235	6100

As shown in Fig. 1(a), the vacuum inner shell used in the experiment is mainly composed of inner wall, outer wall, upper rib plate, middle rib plate and lower rib plate. The inner wall arc length is 695 mm, the outer wall arc length is 795 mm, the inner and outer wall thickness is 10 mm, and the distance is 50 mm, and the thickness of the three ribbed plates is 7 mm.
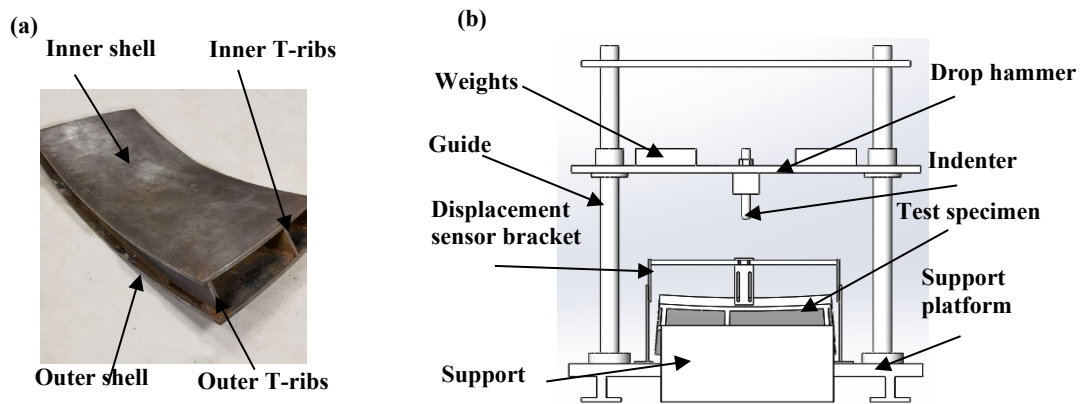

Fig. 1. Experimental specimen and low speed impact falling weight experimental device. (a) Experimental specimen. (b) Low speed impact falling weight experimental device.

Fig. 1(b) shows the experimental device and the components of the sketch. The drop hammer is guided vertically by two guide rails. These two parts are connected by ball bearings, and two standard weight can be fixed above the plate to change the mass of the falling weight. The vacuum inner shell is placed in the center of the test bench through two supports, and rigid constraints are set at both ends. The impact head uses a pressure sensor with hemispherical body, which is installed in the center of the slider. The displacement sensor is fixed above the vacuum inner shell with a bracket. The signal acquisition includes pressure signal acquisition, displacement signal acquisition and image acquisition. The image acquisition is realized by the Thousand Eye Wolf 2F01M high-speed camera. The pressure signal is transmitted through the BLSM sensor, with a testing range of 20000N. The small displacement sensor in the installation space of the impact head is the Miran KTR11 linear displacement sensor, with a range of 0-15 mm. The signal acquisition is realized by the Siemens S7 1200 programmable logic controller (PLC). The whole test process includes three steps.

1) Place the displacement sensor near the impact position, so that the displacement sensor is as close to the impact position as possible without interference with the indenter. Then connect the PLC with the displacement sensor and pressure sensor. Then adjust the high-speed camera, open the high-speed camera program, and adjust the position and focal length of the high-speed camera so that it can clearly capture the process of low-speed impact.

2) Place the corresponding standard weight above the falling weight and mark the height of the falling weight. In this experiment, set the heights of 300 mm, 400 mm, 500 mm and 600 mm respectively, and record them as four energy levels E1, E2, E3 and E4. Each energy level is subject to five groups of tests.

3) Release the falling weight from the specified height along the guide rail. In the process of energy transmission of the sample, the falling hammer will rebound several times. Finally, when the falling hammer is completely stationary, lift it to a certain height to release the remaining elastic deformation energy of the inner shell.

Experimental data discussion. 1) Impact energy. The height of the free falling body is divided into four grades. Therefore, without changing the mass of the falling hammer, the impact energy is also divided into four grades. First, two standard weights are placed, and then the mass of the impact block is added, the total is 28.4 kg, and the impact energy is 83.496 J, 111.328 J, 139.16 J, 166.992 J respectively.

2) Energy absorption rate of impact specimen. During the impact process, because the impact specimen is completely fixed, the kinetic energy generated during the falling process of the impact head will be transferred to the impact specimen, and then rebound itself. In the case of ignoring friction, at this time, the energy is only transferred between the impact head and the vacuum inner shell. The energy absorbed by the impact specimen can be obtained by subtracting the potential energy at the highest rebound point from the potential energy at the starting highest point of the impact head, This data is used to quantify the energy absorption capacity of the impact specimen and the impact response when bearing the impact of different energy levels.

3) Impact force and impact response displacement. Through the obtained data, we can analyze the relationship between the impact force and the vacuum inner shell deformation with the increase of energy level under different impact energy, and whether there is a functional relationship between them.

4) Other data. It mainly includes the impact speed, rebound speed and rebound displacement of the impact head in the falling stage. These data are mainly used to describe the impact process and calculate the previous data. The data acquisition method is to capture the impact and rebound process of the impact head through the high-speed camera, and then use the high-speed video target tracking measurement software to show the whole impact process by setting the trajectory of the tracking impact head, and draw the speed change curve through the software's own function.

There are four energy levels in total, and five groups of experiments are conducted for each level. The impact forces of the four energy levels are respectively expressed by F1,F2,F3,F4. The impact forces obtained are shown in Table 2. the impact response displacement of the four energy levels shall be represented by S1, S2, S3 and S4 respectively.

The average impact force of the four energy levels is 669.9219 N, 825.1736 N, 1054.36 N and 1253.42 N respectively. It can be found that as the impact height increases, the impact force will also increase. Under the same conditions of E1 energy level, the impact force on the segment changes gently, and under the same conditions of E2 and E3 energy levels, the impact force on the segment changes gradually. Under the same conditions of E4 energy level, the impact force changes obviously.

The impact response displacement under each group of energy levels is shown in the table above. The average value of impact response displacement is 0.026552 mm, 0.042558 mm, 0.056368 mm and 0.077706 mm respectively. With the gradual increase of impact energy, the impact response displacement increases, and the variation fluctuation of impact response displacement also increases. From the distribution relationship between the average value of impact force and impact response displacement of each group, the impact force is positively correlated with the impact displacement response, which indicates that the concave structure of the specimen has good impact resistance and excellent energy absorption performance.

From the above two sets of data, the impact force generated by the slider and the impact response displacement of the vacuum inner shell are roughly distributed in a relatively closed range. There are two main reasons for the same test error. First, because the range of the impact

head is large, and the measured data is relatively small, which will magnify the test error. The second is the error caused by the flatness of the specimen itself and the flatness of the installation.

Table 2. Impact force results.

Group number	F_1(N)	S_1(mm)	F_2(N)	S_2(mm)	F_3(N)	S_3(mm)	F_4(N)	S_4(mm)
1	640.1476	0.02645	831.5538	0.04024	1027.922	0.05435	1310.07	0.08343
2	684.1002	0.02452	797.5261	0.04364	1025.798	0.05435	1186.72	0.07823
3	671.3397	0.02848	798.2350	0.03971	1119.464	0.05208	1209.641	0.07235
4	674.8843	0.02566	895.3559	0.04356	1086.054	0.06123	1209.557	0.07217
5	679.1377	0.02765	803.1973	0.04564	1012.562	0.05983	1351.112	0.08235

The low speed impact process can be recorded with a high-speed camera. After recording the speed of each frame rate, take the average value of each group of impact speed under the same energy level, and draw a speed frame rate diagram, as shown in Fig. 2. According to the height of free fall, the collision velocities of the four energy levels are 2.42 m/s, 2.8 m/s, 3.13 m/s and 3.43 m/s respectively. The collision velocities obtained by the high-speed camera are 2.42 m/s, 2.78 m/s, 3.21 m/s and 3.40 m/s respectively, and the error is within 5%. The results of the high-speed camera are available.
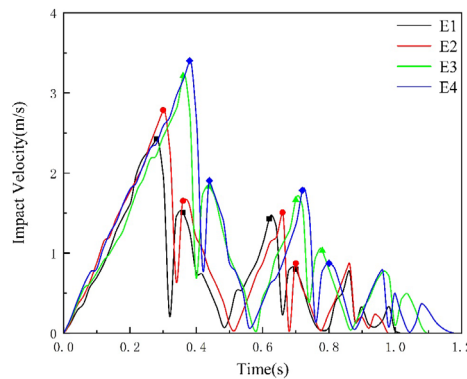

Fig. 2. Experimental speed frame rate diagram from high-speed camera.

With the increase of energy levels, the time of wave peaks successively moves backward, but the phase difference of wave length of each energy level curve is small. The height of the second wave peak and the third wave peak are basically the same, and the two represent the first rebound speed and the second collision speed respectively, indicating that the energy loss in the impact process can be basically ignored. Through the first impact speed and the first rebound speed, the energy absorption rate of the vacuum chamber wall can be obtained, as shown in the Table 3.

Table 3. Energy absorption rate of inner wall under different energy levels.

Energy level	First impact velocity(m/s)	First bounce velocity(m/s)	Energy absorption rate
E1	2.4256	1.6993	50.92%
E2	2.7865	1.854	55.73%
E3	3.2135	2.0581	58.98%
E4	3.4025	2.1449	60.26%

The change trend of the energy absorption rate increases with the increase of the energy level, the damage level will increase correspondingly, and the performance degradation of the sample will occur. Therefore, the rebound amount cannot cause a linear increase in the value with the linear increase of the energy level, so the result shows a positive correlation between the energy absorption rate and the impact energy level.

Simulation Research

The energy absorption rate under four energy levels is analyzed through finite element software, energy absorption rate simulating results under four energy levels were listed in Table 4.

Table 4. Energy absorption rate of vacuum chamber wall through simulation.

Energy level	Total energy(J)	Residual energy of impact block(J)	Energy absorption rate
E1	82.925	50.573	39.02%
E2	11.101	61.047	45.01%
E3	138.72	68.766	50.43%
E4	166.59	74.8	55.10%

The comparison of the energy absorption rate of the vacuum chamber wall between the experiment and the simulation is shown in Fig. 3. With the rise of the energy level, the energy absorption rate of the vacuum chamber wall gradually increases, and the change speed of the E1, E2, E3 energy absorption rate is consistent with the simulation results, but the experimental energy absorption rate is larger than the simulation results because the various collision speed is used to calculate the energy absorption rate. It does not mean that the vacuum chamber wall completely absorbs the remaining energy.
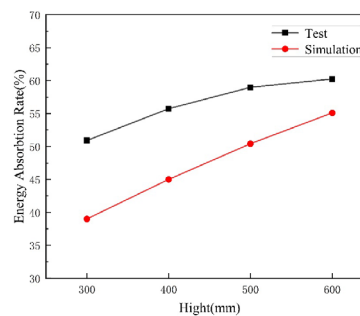

Fig. 3. Comparison of energy absorption rate of vacuum chamber wall between experiment and simulation.

In the experiment, the overall collision rebound caused by the unstable fixation of the vacuum chamber wall and the force of the support on the ground will also cause the loss of energy, resulting in the large value of the energy absorption rate in the experimental results.

The rib plate is an indispensable part of the vacuum chamber welding process, which plays a role in supporting the whole and strengthening the stability. Due to the limitations of the experimental device, it is temporarily impossible to analyze the influence of the rib plate on the whole vacuum chamber in mechanical straightening. The simulation software is used to act the impact energy on the positions close to the lower rib plate and the upper rib plate respectively to analyze the role of the rib plate in the correction of deformation.

When the impact position is close to the vertical ribs, the center and away from the outer T-ribs plate, the different deformation diagrams of the vacuum chamber wall were shown in Fig. 4.

respectively. It can be seen that the closer the collision center is to the position of the outer T-ribs in Fig. 4(a), the smaller the deformation under the same impact energy. The reason is that although the impact energy acts on the middle rib plate and the vertical ribs as shown in Fig. 4(c), the two rib plates are shorter than outer T-ribs, so the outer T-ribs plays a major role in resisting deformation in the inner wall of this vacuum chamber, and the deformation is proportional to the distance from the outer T-ribs.
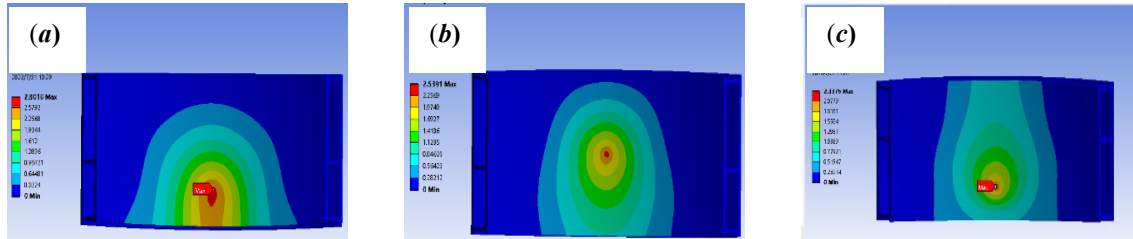

Fig. 4. The deformation diagram of the vacuum chamber wall when the impact position is close to the vertical ribs. (a) close to outer T-ribs (b) center (c) away from outer T-ribs.

Conclusion

In this paper, the impact response of vacuum chamber wall under low-speed impact is studied through experiments and simulation analysis. The following conclusions are drawn,

1) When the yield does not occur, the impact response displacement is positively correlated with the impact energy, and between different energy levels, with the increase of the energy level, the fluctuation of the impact force curve also gradually increases.

2) The change trend of the energy absorption rate of the wall in the vacuum chamber increases with the increase of the energy level, indicating that when the impact energy level increases, the damage level will increase correspondingly, and the performance of the sample will deteriorate. Therefore, the rebound amount cannot cause a linear increase in the value with the linear increase of the energy level, and the result shows a positive correlation between the energy absorption rate and the impact energy level.

3) According to the simulation results, the energy absorption rate of the vacuum chamber wall is relatively small, but the change trend is consistent with the experiment. The principle is that part of the energy makes the vacuum chamber wall rebound and act on the support as a whole during the experiment.

4) The rib plate plays a key role in the mechanical correction of vacuum chamber. The deformation under impact energy is proportional to the distance from the rib plate.

Declaration of competing interest

The authors declare that they have no known competing financial interests or personal relationships that could have appeared to influence the work reported in this paper.

Acknowledgments

References

[1] J. Zheng, J. Qin, K. Lu, M. Xu, X. Duan, G. Xu, J. Hu, X. Gong, Q. Zang, Z. Liu, L. Wang, R. Ding, J. Chen, P. Li, L. Xue, L. Cai, Y. Song, Recent progress in Chinese fusion research based on superconducting tokamak configuration, The Innovation 3 (2022) 100269. https://doi.org/10.1016/j.xinn.2022.100269

[2] P.V.E. McClintock, Controlled thermonuclear fusion, by Jean Louis Bobin, Contemporary Physics 58 (2017) 1-100.

[3] Y.T. Song, S.T. Wu, J.G. Li, B.N. Wan, P. Fu, M.Y. Ye, J. Zheng, K. Lu, X. Gao, S.M. Liu, X.F. Liu, M. Lei, X.B. Peng, Y. Cheng, Concept design of CFETR tokamak machine, IEEE T. Plasma Sci. 42 (2014) 503-509. https://doi.org/10.1109/TPS.2014.2299277

[4] M. Jianguo, W. Jiefeng, L. Zhihong, R&D of full-scale partial vacuum vessel mockup for future fusion engineering test reactor in China, J. Fusion Energy 34 (2015) 666-670.

[5] K. Masaki, Y.K. Shibama, S. Sakurai, K. Shibanuma, A. Sakasai, JT-60SA vacuum Vessel manufacturing and assembly, Fusion Eng. Des. 87 (2012) 742-746. https://doi.org/10.1016/j.fusengdes.2012.02.014

[6] L. Xiu, J. Wu, Z. Liu, J. Ma, X. Fan, H. Ji, X. Xia, Y. Li, Weld distortion prediction of the CFETR vacuum vessel by inherent strain theory, Fusion Eng. Des. 121 (2017) 43-49. https://doi.org/10.1016/j.fusengdes.2017.03.175

[7] Z. Chen, Z. Chen, R.A. Shenoi, Influence of welding sequence on welding deformation and residual stress of a stiffened plate structure, J. Ocean Eng. 106 (2015) 271-280. http://dx.doi.org/10.1016/j.oceaneng.2015.07.013

[8] J. Ordieres, E. Rodríguez, A. Bayón, J. Caixas, A. Barbensi, P. Guglielmi, Improvement of manufacturing jigs design for reduction of welding distortion in Vacuum Vessel PS1 through finite element analysis, Fusion Eng. Des. 146 (2019) 2168–2171. https://doi.org/10.1016/j.fusengdes.2019.03.141

[9] H. Ji, X. Xia, J. Wu, H. Wu, Z. Liu, J. Ma, Z. Liu, X. Shen, Welding technology development for the fabrication of vacuum vessel for CFETR, Fusion Eng. Des. 147 (2019) 111272. https://doi.org/10.1016/j.fusengdes.2019.111272

[10] P.Y. Lee, B.L Hou, G.D. Jian, et al. Redesign of gravity support system for ITER construction. Fusion Eng. Des. 85 (2010) 33-38.

[11] Y. Zhai, B. Huang, J. Zhang, B. Zhang, S. Liu, Q. Huang, Effect of weld spacing on microstructure and mechanical properties of CLAM electron beam welding joints, Fusion Eng. Des. 112 (2016) 440-449. https://doi.org/10.1016/j.fusengdes.2016.06.027

[12] B. Li, S.N. Melkote, Fixture clamping force optimisation and its impact on workpiece location accuracy, Int. J. Adv. Manuf. Technol. 17 (2001) 104-113. https://doi.org/10.1007/s001700170198

[13] H. Ji, J. Wu, H. Wu, Z. Liu, J. Ma, X. Fan, Analysis of welding deformation on CFETR 1/32 vacuum vessel mockup, Fusion Eng. Des. 144 (2019) 160-163. http://dx.doi.org/10.1016/j.fusengdes.2019.05.012

[14] R. Wang, Z. Liu, J. Wu, B. Jiang, B. Li, Design of DMA probe for the ultrasonic testing of CFETR vacuum vessel weld, Fusion Eng. Des. 146 (2019) 987-990. https://doi.org/10.1016/j.fusengdes.2019.01.136

[15] R. Wang, Z. Liu, J. Wu, B. Jiang, B. Li, Research on phased array ultrasonic testing on CFETR vacuum vessel welding, Fusion Eng. Des. 139 (2019) 124-127. https://doi.org/10.1016/j.fusengdes.2019.01.050

[16] Y. Noguchi, M. Tsunokai, K. Nakata, N. Takeda, Applicability of eddy current technique in in-bore NDT tool for ITER hydraulic pipe welds, Fusion Eng. Des. 146 (2019) 2571-2576. https://doi.org/10.1016/j.fusengdes.2019.04.044

[17] G. D'Amico, J. Caixas, A. LoBue, A. Bayon, In-process control of ITER vacuum vessel PS1 welding jig by means of FEM simulation and welding distortion analysis, Fusion Eng. Des. 146 (2019) 1843-1847. https://doi.org/10.1016/j.fusengdes.2019.03.048

[18] J. Caixas, J. Guirao, A. Bayon, L. Jones, J.F. Arbogast, A. Barbensi, A. Dans, A. Facca, E. Fernandez, J. Fernández, S. Iglesias, M. Jimenez, P. Jucker, G. Micó, J. Ordieres, J.M. Pacheco, R. Paoletti, G.P. Sanguinetti, V. Stamos, M. Tacconelli, Weld distortion prediction of the ITER vacuum vessel using finite element simulations, Fusion Eng. Des. 88 (2013) 2011-2014. https://doi.org/10.1016/j.fusengdes.2013.02.101

[19] J. Zhang, L. Yu, Y. Liu, H. Li, C. Liu, J. Wu, J. Ma, Z. Li, Effect of welding sequences on the welding stress and distortion in the CFETR vacuum vessel assembly using finite element simulation, Int. J. Pres. Ves. Pip. 175 (2019) 103930. https://doi.org/10.1016/j.ijpvp.2019.103930